

# Global variational approach to elliptic transport barriers in three dimensions

David Oettinger, Daniel Blazeovski, and George Haller<sup>a)</sup>

*Institute of Mechanical Systems, Department of Mechanical and Process Engineering, ETH Zürich, Leonhardstrasse 21, 8092 Zürich, Switzerland*

(Received 24 September 2015; accepted 11 March 2016; published online 24 March 2016)

We introduce an approach to identify elliptic transport barriers in three-dimensional, time-aperiodic flows. Obtained as Lagrangian Coherent Structures (LCSs), the barriers are tubular non-filamenting surfaces that form and bound coherent material vortices. This extends a previous theory of elliptic LCSs as uniformly stretching material surfaces from two-dimensional to three-dimensional flows. Specifically, we obtain explicit expressions for the normals of pointwise (near-) uniformly stretching material surfaces over a finite time interval. We use this approach to visualize elliptic LCSs in steady and time-aperiodic ABC-type flows. © 2016 AIP Publishing LLC.

[<http://dx.doi.org/10.1063/1.4944732>]

**Even complex flows tend to produce organized tracer patterns. Designed as generalizations of invariant manifolds to finite-time dynamical systems with arbitrary time dependence, Lagrangian Coherent Structures (LCSs) are special material surfaces that act as transport barriers, guiding the formation of these directly observable tracer patterns. Notably, outermost elliptic LCSs demarcate the boundaries of coherent material vortices in fluid flows. Here, we extend a recent theory of elliptic LCSs from two- to three-dimensional flows and use it to uncover elliptic LCSs in steady and temporally aperiodic flow models.**

## I. INTRODUCTION

Transport barriers provide a simplified picture of complex time-aperiodic flows as surfaces underlying the formation of tracer patterns.<sup>16</sup> Application areas include fluid dynamics,<sup>6</sup> geophysical flows,<sup>23,25</sup> and chemical reactions.<sup>21,24</sup>

An indirect approach to locating transport barriers is to partition the flow into coherent sets.<sup>11</sup> Obtained from a probabilistic transfer operator, coherent sets exhibit minimal leakage among each other. In contrast to the methods that we outline in the following, set-based approaches<sup>3,11,14</sup> identify patches and volumes formed by coherent sets of trajectories.

Another, direct approach to transport barriers targets evolving material surfaces with distinguished dynamical behavior. These LCSs (see Ref. 16 for a review) can be located as explicitly parametrized curves or surfaces using recent variational methods.<sup>2,7,15,17</sup> Three types of LCSs have been introduced in these works: Parabolic LCSs for identifying jet-type structures,<sup>7</sup> hyperbolic LCSs as generalized normally hyperbolic invariant manifolds,<sup>15</sup> and elliptic LCSs capturing coherent Lagrangian vortices.<sup>17</sup> The latter can be envisioned as sharp material tubes that guide coherent motion of matter over a prolonged interval of time, as often observed, e.g., in tornadoes, steam rings, or ocean eddies. In

an idealized setting, similar objects exist in steady, incompressible Euler flows,<sup>1,4</sup> in the form of invariant tori or cylinders.

All of the aforementioned variational LCS approaches<sup>7,15,17</sup> provide parametrizations of LCS surfaces. These parametrized surfaces are obtained by solving differential equations, as opposed to merely thresholding scalar fields. Moreover, the variational principles underlying the methods in Refs. 7 and 17 explicitly define the global deformation properties of the surfaces they highlight.

Methods for hyperbolic and elliptic LCSs have recently been extended to three-dimensional flows.<sup>2</sup> These local variational techniques render LCSs as surfaces orthogonal to directions of maximal normal repulsion (hyperbolic LCSs) and maximal tangential shear (elliptic LCSs).

Strictly shear-maximizing elliptic LCSs,<sup>2</sup> however, tend to be difficult to locate in real-life data sets, such as the Southern Ocean State Estimate.<sup>22</sup> This is due to the idealized nature of these LCSs, requiring pointwise maximal tangential shear at all points of the surface. This strict maximality requirement may not yield tubular surfaces in complex and noisy data sets.

Here, we propose a complementary approach to elliptic LCSs in three-dimensional flows. Our method is an extension of the most recent global variational theory of elliptic LCSs in two-dimensional flows,<sup>17</sup> which has already been applied to various numerical velocity fields.<sup>13,17,19,31</sup> The proposed approach replaces the requirement of pointwise maximal tangential shear for elliptic LCSs<sup>2</sup> with the requirement of near-uniform stretching along the LCSs. This allows for small variations in the uniformity of the stretching, thereby yielding numerically more robust elliptic LCS surfaces.

After introducing the mathematical setting, we review the theory of elliptic LCSs in two-dimensional flows from Ref. 17. This approach identifies vortex boundaries as closed material curves that, over a finite time interval, uniformly stretch by a factor  $\lambda$  near unity. By directly extending this variational principle to three dimensions, we find that the generalization of closed and uniformly  $\lambda$ -stretching curves to

<sup>a)</sup>georgehaller@ethz.ch

$\lambda$ -stretching tubular *surfaces* is not straightforward. Our considerations, however, suggest seeking pointwise near-uniformly stretching surfaces. In contrast to the maximal-shear method for elliptic LCSs in three dimensions,<sup>2</sup> seeking near-uniformly stretching surfaces yields a parametric family of admissible normal fields for the LCSs. It turns out that, at each point, all near-uniformly stretching surfaces necessarily contain the intermediate eigenvector of the right Cauchy-Green strain tensor. This observation simplifies the construction of elliptic LCSs as tubular near-uniformly stretching surfaces. We finally apply this approach to steady and time-periodic ABC-type flows.

## II. SETUP AND NOTATION

We consider non-autonomous ordinary differential equations of the form

$$\dot{x} = u(x, \tau), \quad x \in U, \quad \tau \in [t_0, t], \quad (1)$$

where the flow domain  $U \subset \mathbb{R}^d$  is an open and bounded subset with  $d = 2$  or  $d = 3$ ;  $[t_0, t]$  is a finite time interval; and the velocity field  $u : U \times [t_0, t] \rightarrow \mathbb{R}^d$  is assumed to be smooth. In Sec. III, we consider  $d = 2$ , and from Sec. IV onwards, we take  $d = 3$ . We denote trajectories passing through a point  $x_0 \in U$  at time  $t_0$  by  $x(\tau; t_0, x_0)$ . For any time  $\tau \in [t_0, t]$ , we define the flow map as  $F_{t_0}^\tau(x_0) := x(\tau; t_0, x_0)$ .

Consider a set of initial positions forming a codimension-one surface  $\mathcal{M}(t_0)$  at time  $t_0$ . Its time- $\tau$  image,  $\mathcal{M}(\tau)$ , termed a *material surface*, is obtained under the flow map, i.e.,  $\mathcal{M}(\tau) = F_{t_0}^\tau(\mathcal{M}(t_0))$ . While any material surface divides locally the extended phase space, only special material surfaces with sustained coherence in time will act as transport barriers.<sup>2</sup>

We proceed by defining the Cauchy-Green strain tensor field

$$C_{t_0}^t(x_0) := [DF_{t_0}^t(x_0)]^T DF_{t_0}^t(x_0), \quad (2)$$

with  $DF_{t_0}^t(x_0)$  denoting the Jacobian matrix of  $F_{t_0}^t$  expressed in the standard Euclidean basis, and the  $T$ -superscript referring to transposition (see Ref. 20 for the formulation on Riemannian manifolds). At each  $x_0$ ,  $C_{t_0}^t(x_0)$  is a symmetric and positive definite matrix. In two dimensions,  $C_{t_0}^t(x_0)$  has two positive eigenvalues

$$0 < \lambda_1(x_0) \leq \lambda_2(x_0).$$

Unless the two eigenvalues are equal, the associated unit eigenvectors  $\xi_{1,2}(x_0)$  form a well-defined, orthonormal basis. In three dimensions,  $C_{t_0}^t(x_0)$  has three positive eigenvalues  $\lambda_{1,2,3}(x_0)$ , which we order as

$$0 < \lambda_1(x_0) \leq \lambda_2(x_0) \leq \lambda_3(x_0).$$

For incompressible flows, the product of the eigenvalues is unity, i.e.,  $\lambda_1(x_0) \cdot \lambda_2(x_0) \cdot \lambda_3(x_0) = 1$ . Except at points  $x_0 \in U$  where the eigenvalues of  $C_{t_0}^t(x_0)$  are repeated, i.e.,  $\lambda_1(x_0) = \lambda_2(x_0)$  or  $\lambda_2(x_0) = \lambda_3(x_0)$ , the unit eigenvectors  $\xi_1(x_0)$ ,  $\xi_2(x_0)$ , and  $\xi_3(x_0)$  again form an orthonormal basis. Pointwise, we orient them so that  $\xi_3(x_0) = \xi_1(x_0) \times \xi_2(x_0)$ .

## III. REVIEW OF ELLIPTIC LAGRANGIAN COHERENT STRUCTURES IN TWO DIMENSIONS

Following the two-dimensional approach introduced in Ref. 17, consider a closed material curve of initial particle positions  $\gamma(t_0)$ . Over the finite time interval  $[t_0, t]$ , the averaged relative tangential stretching of  $\gamma(t_0)$  is given by the strain functional

$$Q(\gamma(t_0), t) = \oint_{\gamma(t_0)} \sqrt{\frac{\langle x_0'(s), C_{t_0}^t(x_0(s))x_0'(s) \rangle}{\langle x_0'(s), x_0'(s) \rangle}} ds, \quad (3)$$

where  $x_0(s)$  is a parameterization of  $\gamma(t_0)$ ,  $x_0'(s) = dx_0/ds$  is the (non-unit) tangent vector to  $\gamma(t_0)$ , and  $\langle \cdot, \cdot \rangle$  denotes the Euclidean inner product.

Stationary curves of the functional  $Q$  defined in (3) do not, by definition, exhibit leading-order variation in the averaged tangential strain. They are, therefore, non-filamenting curves that can be used to define *elliptic Lagrangian Coherent Structures*.<sup>17</sup> Mathematically, these elliptic LCSs solve the classic Euler-Lagrange equation associated with the Lagrangian

$$q(x_0, x_0') = \sqrt{\frac{\langle x_0', C_{t_0}^t(x_0)x_0' \rangle}{\langle x_0', x_0' \rangle}}.$$

The Lagrangian  $q(x_0, x_0')$  has no explicit dependence on the curve parameter  $s$  and hence, by Noether's theorem,<sup>12</sup> produces a first integral  $I$  for the Euler-Lagrange equation associated with the variational problem  $\delta Q(\gamma, \cdot) = 0$ . Evaluated on stationary curves of  $Q$ , the first integral is of the form

$$I = q - \langle x_0', \partial_{x_0'} q \rangle = q = \text{const.} \quad (4)$$

Denoting the constant in (4) by  $\lambda$ , we obtain that  $q = \lambda$ , which we rewrite as

$$\langle x_0'(s), C_{t_0}^t(x_0(s))x_0'(s) \rangle = \lambda^2 \langle x_0'(s), x_0'(s) \rangle. \quad (5)$$

Expressing (5) in the eigenbasis of  $C_{t_0}^t(x_0)$ , one finds that closed stationary curves of  $Q$  are closed integral curves of the vector fields

$$\eta_\lambda^\pm(x_0) = \sqrt{\frac{\lambda_2(x_0) - \lambda^2}{\lambda_2(x_0) - \lambda_1(x_0)}} \xi_1(x_0) \pm \sqrt{\frac{\lambda^2 - \lambda_1(x_0)}{\lambda_2(x_0) - \lambda_1(x_0)}} \xi_2(x_0). \quad (6)$$

As these curves satisfy (5) at each point, they are guaranteed to stretch uniformly by a factor of  $\lambda$ . For such a curve, denoted by  $\gamma(t_0)$ , the stretching factor  $\lambda$  is a positive number between  $\max_{x_0 \in \gamma(t_0)} \sqrt{\lambda_1(x_0)}$  and  $\min_{x_0 \in \gamma(t_0)} \sqrt{\lambda_2(x_0)}$ . In the particular case of  $\lambda = 1$ , these stationary curves of  $Q$  experience no stretching between the times  $t_0$  and  $t$ . We refer to this case of perfect coherence as *neutral stretching*.

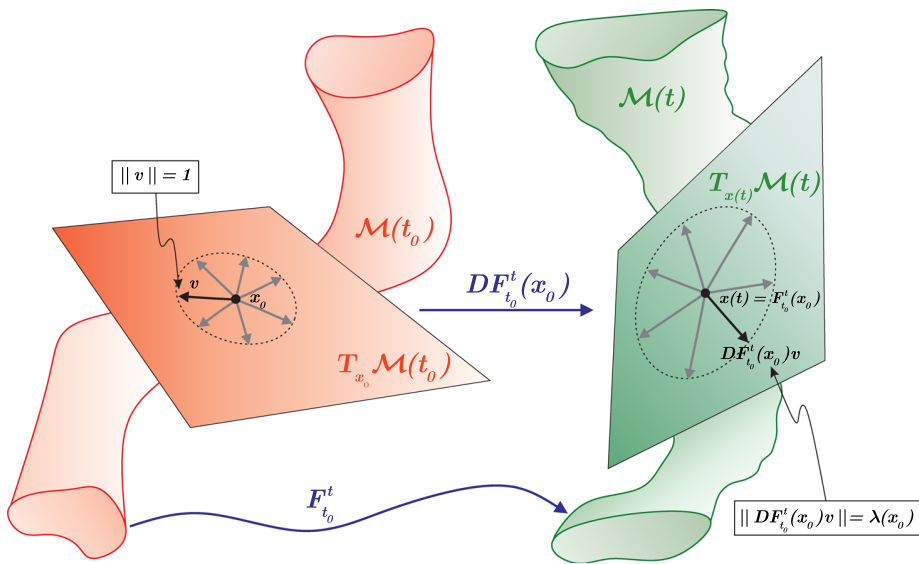


FIG. 1. Illustration of a tubular pointwise uniformly stretching surface as introduced in Definition 1.

### IV. UNIFORMLY AND NEAR-UNIFORMLY STRETCHING MATERIAL SURFACES IN THREE-DIMENSIONAL FLOWS

#### A. Uniform stretching in three-dimensional flow

As outlined above, in two dimensions, elliptic LCSs are non-filamenting, closed material curves that are infinitesimally  $\lambda$ -stretching. A straightforward generalization to three dimensions is to seek two-dimensional tubular surfaces that are uniformly stretching by a factor of  $\lambda$  along all directions in each of their tangent spaces. We now explore this idea in detail.

**Definition 1.** A smooth material surface  $\mathcal{M}(\tau)$  is *pointwise uniformly stretching* if, under advection from time  $t_0$  to  $t$ , all vectors in each tangent space  $T_{x_0}\mathcal{M}(t_0)$  stretch uniformly by the same factor  $\lambda(x_0) \in [\sqrt{\lambda_1(x_0)}, \sqrt{\lambda_3(x_0)}]$ .

We illustrate the basic idea of Definition 1 in Figure 1. The definition translates to the explicit requirement that

$$\sqrt{\frac{\langle v, C_{t_0}^t(x_0)v \rangle}{\langle v, v \rangle}} = \lambda(x_0), \quad \forall x_0 \in \mathcal{M}(t_0), \forall v \in T_{x_0}\mathcal{M}(t_0). \tag{7}$$

**Theorem 1.** *In three-dimensional flow, as given by (1) with  $d=3$ , any pointwise uniformly stretching material surface  $\mathcal{M}(\tau)$  would have to satisfy  $\lambda(x_0) = \sqrt{\lambda_2(x_0)}$ .*

*Proof.* Consider an arbitrary pointwise uniformly stretching surface  $\mathcal{M}(\tau)$ . At any point  $x_0 \in \mathcal{M}(t_0)$  where  $C_{t_0}^t$  has distinct eigenvalues, we examine the condition for pointwise uniform stretching (7) by considering an arbitrary

tangent vector  $v \in T_{x_0}\mathcal{M}(t_0)$ . Dropping the position argument for brevity, we use the eigenbasis  $\xi_{1,2,3}$  to write  $v = \alpha\xi_1 + \beta\xi_2 + \gamma\xi_3$ . By orthonormality of the  $\xi_{1,2,3}$ , (7) then becomes  $\alpha^2\lambda_1 + \beta^2\lambda_2 + \gamma^2\lambda_3 = \lambda^2(\alpha^2 + \beta^2 + \gamma^2)$ , or equivalently

$$\alpha^2(\lambda^2 - \lambda_1) + \beta^2(\lambda^2 - \lambda_2) + \gamma^2(\lambda^2 - \lambda_3) = 0. \tag{8}$$

As shown in Table I, condition (8) only provides full linear spaces of solutions for  $\lambda = \sqrt{\lambda_2}$  (case 3). Here, the solution set of (8) consists of two planes (cf. Fig. 2(b)). For a generic choice of  $\lambda$ , on the other hand, the solution set of (8) is a double cone (cases 2 and 4 in Table I). In the remaining two cases of  $\lambda = \sqrt{\lambda_1}$  and  $\lambda = \sqrt{\lambda_3}$ , the solution set of (8) is a line (cases 1 and 5 in Table I). The tangent plane  $T_{x_0}\mathcal{M}(t_0)$ , therefore, has to coincide with one of the two planes obtained for  $\lambda = \sqrt{\lambda_2}$  (case 3). (For points where  $C_{t_0}^t$  has repeated eigenvalues, see Appendix B.)  $\square$

*Remark 1.* As opposed to the neutral stretching  $\lambda = 1$  in two dimensions, the three-dimensional analogue of neutral stretching is  $\lambda(x_0) = \sqrt{\lambda_2(x_0)}$ , representing the only case that allows for the construction of a pointwise uniformly stretching surface  $\mathcal{M}(\tau)$ . Viewed globally, however, these surfaces cannot be expected to stretch uniformly, since their pointwise stretching factor  $\sqrt{\lambda_2(x_0)}$  generally varies in space. The uniformity in stretching refers to their tangent spaces only and should therefore be viewed as a local property.

*Remark 2.* In order to construct a *globally* uniformly stretching surface, by Theorem 1, we would need to find a

TABLE I. Solution sets of (8) depending on the choice of  $\lambda$ .

| Case | Values of $\lambda$                             | Geometry of solution set of (8)                                      |
|------|---|--|
| 1    | $\lambda = \sqrt{\lambda_1}$                    | $\xi_1$ -axis (cf. Fig. 2(a), Appendix A)                            |
| 2    | $\sqrt{\lambda_1} < \lambda < \sqrt{\lambda_2}$ | Elliptic double cone about $\xi_1$ -axis (cf. Fig. 2(a), Appendix C) |
| 3    | $\lambda = \sqrt{\lambda_2}$                    | Two planes (cf. Fig. 2(b), Appendix A)                               |
| 4    | $\sqrt{\lambda_2} < \lambda < \sqrt{\lambda_3}$ | Elliptic double cone about $\xi_3$ -axis (cf. Fig. 2(c), Appendix C) |
| 5    | $\lambda = \sqrt{\lambda_3}$                    | $\xi_3$ -axis (cf. Fig. 2(c), Appendix A)                            |

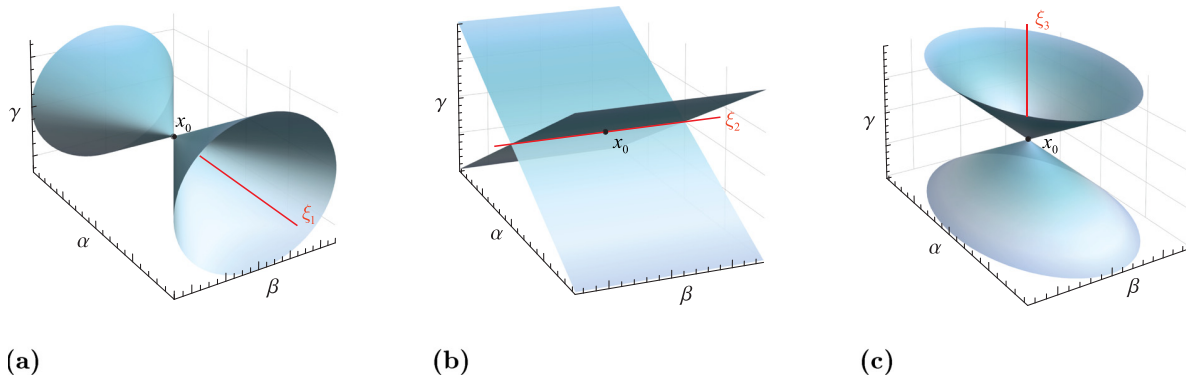


FIG. 2. Directions of  $\lambda$ -stretching for cases 2, 3, and 4 in Table I. (a) Case 2:  $\lambda$ -stretching directions forming a double cone for  $\lambda \in (\sqrt{\lambda_1}, \sqrt{\lambda_2})$ . (b) Case 3: Two planes formed by  $\lambda = \sqrt{\lambda_2}$ -stretching directions. (c) Case 4:  $\lambda$ -stretching directions forming a double cone for  $\lambda \in (\sqrt{\lambda_2}, \sqrt{\lambda_3})$ .

pointwise  $\lambda(x_0)$ -stretching surface whose intersection with a particular level set of  $\lambda_2(x_0)$  is still a two-dimensional surface. There is generally no reason for this to hold, so we will always consider material surfaces  $\mathcal{M}(\tau)$  that are *pointwise* uniformly stretching with a spatially dependent factor  $\lambda(x_0) = \sqrt{\lambda_2(x_0)}$ . (In the following, for brevity, we therefore sometimes omit the “pointwise” attribute.) Such surfaces are of intrinsic interest, as pointwise uniform stretching imposes observable coherence in the deformation of tracer blobs.

*Remark 3.* As we show in Appendix D, for a pointwise uniformly stretching surface  $\mathcal{M}(t_0)$ , all vectors within each tangent space  $T_{x_0}\mathcal{M}(t_0)$  keep their originally enclosed angle when mapped from time  $t_0$  to time  $t$ . They are stretched equally by  $\sqrt{\lambda_2(x_0)}$ , but are otherwise rotated by the same angle. This means that there is no net material shear *within* the tangent space of the surface  $\mathcal{M}(t_0)$  as it evolves into  $\mathcal{M}(t)$ .

*Remark 4.* At any point  $x_0$  of a pointwise uniformly stretching surface  $\mathcal{M}(t_0)$  where  $C_{t_0}^t(x_0)$  has distinct eigenvalues, we find that the surface  $\mathcal{M}(t_0)$  must be normal to one of the two unit vectors

$$n^\pm(x_0) = \sqrt{\frac{\lambda_2(x_0) - \lambda_1(x_0)}{\lambda_3(x_0) - \lambda_1(x_0)}} \xi_1(x_0) \pm \sqrt{\frac{\lambda_3(x_0) - \lambda_2(x_0)}{\lambda_3(x_0) - \lambda_1(x_0)}} \xi_3(x_0) \quad (9)$$

(cf. Appendix A). The vectors  $n^\pm(x_0)$  are precisely the unit normals to the two planes obtained from (8) for the case  $\lambda(x_0) = \sqrt{\lambda_2(x_0)}$ .

**B. Pointwise near-uniformly stretching surfaces**

Based on the considerations above, we seek elliptic LCSs as tubular material surfaces built out of material curves  $\gamma(t_0) \subset \mathbb{R}^3$  that are stationary curves of the functional

$$S(\gamma(t_0), t) = \int_{\gamma(t_0)} \sqrt{\frac{\langle x'_0(s), \tilde{C}_{t_0}^t(x_0(s))x'_0(s) \rangle}{\langle x'_0(s), x'_0(s) \rangle}} ds. \quad (10)$$

Here, the integrand measures how  $\gamma(t_0)$  stretches under the normalized Cauchy-Green tensor

$$\tilde{C}_{t_0}^t(x_0) = \frac{1}{\lambda_2(x_0)} C_{t_0}^t(x_0).$$

This normalization represents a slight modification of the functional introduced earlier in (3), accounting for the fact that the analogue of neutral stretching in three dimensions is given by  $\lambda = \sqrt{\lambda_2}$  (see Remark 1).

By Noether’s theorem,<sup>12</sup> the integrand in (10) is conserved along stationary curves  $x_0(s)$  of  $S$ . Therefore, on these stationary curves, we have

$$\sqrt{\frac{\langle x'_0(s), C_{t_0}^t(x_0(s))x'_0(s) \rangle}{\langle x'_0(s), x'_0(s) \rangle}} = \sqrt{\lambda_2(x_0)(1 + \delta)} =: \lambda(x_0), \quad (11)$$

with the value of the conserved integrand in (10) being equal to the constant value  $\sqrt{1 + \delta}$ . Comparing (11) to (7), we see that stationary curves of  $S$  stretch non-uniformly by  $\lambda(x_0)$ . The constant parameter  $\delta$  measures the deviation of stretching from the value of neutral stretching  $\sqrt{\lambda_2(x_0)}$ .

For a given flow under consideration, one cannot expect that there exists a tubular surface that is precisely pointwise uniformly stretching everywhere ( $\delta = 0$ ). Moreover, even if such a surface existed, unavoidable numerical inaccuracies and sensitivities would render it undetectable. We therefore extend our considerations to surfaces built out of curves that stretch by a factor close to  $\sqrt{\lambda_2}$  ( $|\delta| \ll 1$ ). In general, away from points where  $C_{t_0}^t(x_0)$  has repeated eigenvalues,  $\lambda$ -values satisfying

$$\lambda^2(x_0) = \lambda_2(x_0)(1 + \delta),$$

$$\delta \in \left[ -1 + \frac{\lambda_1(x_0)}{\lambda_2(x_0)} \right) \cup \left( -1 + \frac{\lambda_3(x_0)}{\lambda_2(x_0)} \right],$$

yield elliptic cones of uniform stretching directions, and therefore do not define possible tangent spaces for a  $\lambda$ -stretching surface (cf. Theorem 1). For  $|\delta| \ll 1$ , however, these cones become elongated along the  $\xi_2$ -axis, and hence large subsets of them are  $C^1$ -close to pairs of planes with respective unit normals  $\pm n_\delta^\pm(x_0)$ , where

$$n_\delta^\pm(x_0) = \sqrt{\frac{\lambda_2(x_0)(1 + \delta) - \lambda_1(x_0)}{\lambda_3(x_0) - \lambda_1(x_0)}} \xi_1(x_0) \pm \sqrt{\frac{\lambda_3(x_0) - \lambda_2(x_0)(1 + \delta)}{\lambda_3(x_0) - \lambda_1(x_0)}} \xi_3(x_0). \quad (12)$$

Unless needed, we omit the overall sign for the orientation of the normal direction  $n_\delta^\pm$  in the following. Expression (12) is well-defined for all points  $x_0$  where the Cauchy-Green strain tensor has distinct eigenvalues and  $\delta \in \left[-1 + \frac{\lambda_1(x_0)}{\lambda_2(x_0)}, -1 + \frac{\lambda_3(x_0)}{\lambda_2(x_0)}\right]$ . We illustrate the situation in Fig. 3 and give further details in Appendix C. We point out that by setting  $\delta = 0$  in (12), we recover the pair of planes forming the solution set of (5) for the uniform case  $\lambda(x_0) = \sqrt{\lambda_2(x_0)}$ .

The vectors  $n_\delta^\pm(x_0)$  from (12) turn out to be the optimal choices as normals for surfaces with the smallest possible stretching variations in their tangent spaces:

**Proposition 1.** *At each point  $x_0$  with distinct eigenvalues for  $C_{t_0}^t$ , and for any prescribed value  $\lambda = \sqrt{\lambda_2(1 + \delta)} \in [\sqrt{\lambda_1}, \sqrt{\lambda_3}]$  of stretching, the planes normal to the vectors  $\pm n_{\lambda^2/\lambda-1}^\pm$  defined in (12) experience the smallest possible inhomogeneity in stretching around the value  $\lambda$ . The range of stretching values attained within these planes is the interval  $[\min\{\lambda, \sqrt{\lambda_2}\}, \max\{\lambda, \sqrt{\lambda_2}\}]$ .*

*Proof.* See Appendix E. □

We now use the unit normals  $n_\delta^\pm(x_0)$  (which are optimal in the sense of Proposition 1) to define the most uniformly stretching surfaces possible, along which the stretching of tangent vectors varies by no more than a specified percentage around  $\sqrt{\lambda_2(x_0)}$ . To this end, we introduce a relative stretching variation  $\Delta$ ,  $0 \leq \Delta < 1$ , such that for any  $\delta$

$$\sqrt{\lambda_2}(1 - \Delta) \leq \sqrt{\lambda_2(1 + \delta)} \leq \sqrt{\lambda_2}(1 + \Delta).$$

Restricting ourselves to small  $\Delta$  and allowing  $\delta$  to generally vary along the surface, we introduce the following definition:

**Definition 2.** A smooth material surface  $\mathcal{M}_\Delta(\tau)$  is *pointwise nearly uniformly stretching* with stretching variation  $\Delta$ ,  $0 \leq \Delta \ll 1$ , if for all  $x_0 \in \mathcal{M}_\Delta(t_0)$ , either  $n_{\delta(x_0)}^+(x_0) \perp T_{x_0} \mathcal{M}_\Delta(t_0)$  or  $n_{\delta(x_0)}^-(x_0) \perp T_{x_0} \mathcal{M}_\Delta(t_0)$  holds, with  $\delta(x_0) \in [-2\Delta + \Delta^2, 2\Delta + \Delta^2]$ .

*Remark 5.* In the present study, we seek *elliptic Lagrangian Coherent Structures* as pointwise near-uniformly stretching surfaces (cf. Definition 2). We note that the shear-maximizing material surfaces, used in a previous approach to elliptic LCSs in three dimensions<sup>2</sup> (cf. Sec. I), can also be obtained from normals  $\tilde{n}^\pm$  of the general form  $\tilde{n}^\pm = a\xi_1 \pm b\xi_3$ .

*Remark 6.* Instead of considering variations of closed material curves (10), it would be desirable to derive near-uniformly stretching surfaces (cf. Definition 2) from a variational principle for two-dimensional manifolds with boundary.<sup>30</sup> We expect, however, that such a variational problem would be significantly more difficult than the minimal surface problem (see Ref. 26 for a review). Deriving a general algebraic condition similar to the expression for the surface normal (12) is out of reach here and hence would necessitate a purely numerical approach.

## V. NUMERICAL EXTRACTION OF NEAR-UNIFORMLY STRETCHING SURFACES

### A. Outline of the extraction procedure

Consider being given a three-dimensional velocity field  $u$  (1) over a finite time interval  $[t_0, t]$ . Our goal is to numerically locate elliptic LCSs by seeking time- $t_0$  positions of near-uniformly stretching material surfaces  $\mathcal{M}_\Delta(\tau)$ . Their admissible normals  $n_\delta^\pm$  are given in (12), to be used in a surface-extraction procedure similar to the one in Ref. 2.

The idea behind this procedure is to sample the flow domain using an indexed family of  $N$  reference planes  $(\Pi_i)_{i \in \{1, 2, \dots, N\}}$ , and then assemble each elliptic LCS by computing its intersections with each reference plane  $\Pi \in \{\Pi_i\}$ . Such intersection curves  $x_0(s)$  have tangent vectors that are normal to both  $n_\delta^\pm$  and the normal  $n_\Pi$  of  $\Pi$ . Consequently, the intersection curves are limit cycles of the vector field

$$x'_0 = \eta_{\delta,i}^\pm(x_0) := n_{\Pi_i}(x_0) \times n_\delta^\pm(x_0). \tag{13}$$

Because  $n_\delta^\pm$  are continuous families of direction fields parameterized by  $\delta$ , we need to scan the interval  $\delta \in [-2\Delta + \Delta^2, 2\Delta + \Delta^2]$  to find limit cycles of (13). This procedure typically yields a large number of limit cycles in each reference plane  $\Pi_i$ . The challenge is to combine single limit cycles from each  $\Pi_i$  into a smooth tubular surface  $\mathcal{M}_\Delta(t_0)$ . Moreover, using the Frobenius integrability theorem, one can show that a necessary condition for the existence of a smooth surface  $\mathcal{M}(t_0)$  normal to a smooth vector field  $n$  is that the helicity  $H_n$  of  $n$  vanishes for all points in the surface  $\mathcal{M}(t_0)$ .<sup>2</sup> In our case, with  $n = \pm n_\delta^\pm$  and  $\mathcal{M}(t_0) = \mathcal{M}_\Delta(t_0)$ , the helicity condition reads

$$H_{n_\delta^\pm} = \langle \nabla \times n_{\delta(x_0)}^\pm, n_{\delta(x_0)}^\pm \rangle = 0. \tag{14}$$

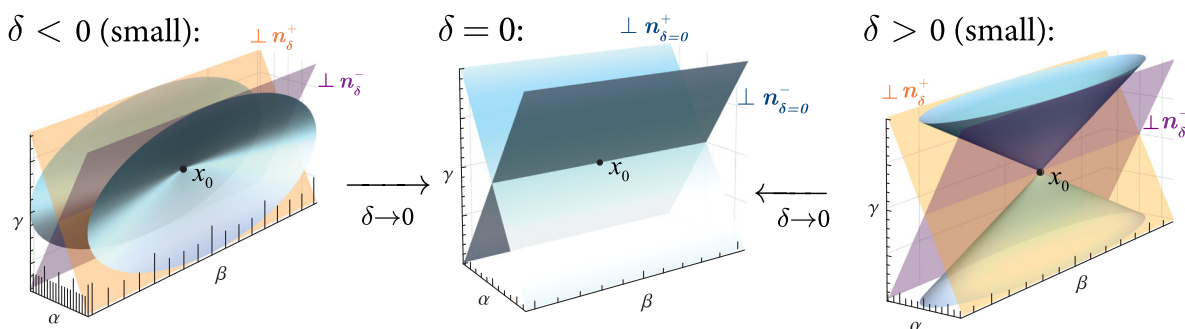


FIG. 3. Elongated elliptic double cones formed by  $\sqrt{\lambda_2(1 + \delta)}$ -stretching directions collapse onto a pair of planes for  $\delta \rightarrow 0$ . As long as  $\delta$  is small, the double cones are well approximated by two planes tangent to them, colored purple and orange here. In Proposition 1, we show that these planes define tangent spaces of surfaces that are pointwise most uniformly stretching, as described in Definition 2. We give the expression for their unit normals  $n_\delta^\pm$  in (12).

Such a helicity condition has already been considered by others<sup>27,29</sup> for the visualization of surfaces approximately perpendicular to an imposed normal field.

We remark that the procedure outlined above requires computing the flow map  $F_{t_0}^t$  and hence the normals  $n_{\delta}^{\pm}$  (12) as fields over the domain of initial positions. In applications where the velocity field  $u$  (1) is given numerically (from either an experiment or a numerical simulation), the resolution of the velocity data therefore needs to be sufficiently high in both space and time.

### B. Selecting closed orbits for the construction of elliptic LCSs

We now explain how to select the closed orbits of  $\eta_{\delta,i}^{\pm}$  needed for constructing an elliptic LCS  $\mathcal{M}_{\Delta}(t_0)$ . Specifically, for a sequence of reference planes  $\Pi_{i_0}, \Pi_{i_0+1}, \dots$ , in each plane  $\Pi_i$ , we need to identify a single optimal limit cycle of  $\eta_{\delta,i}^{\pm}$  (labeled  $\gamma_i$ ). We do this by introducing an auxiliary surface  $\mathcal{S}(t_0)$ , and, for each plane  $\Pi_i$ , selecting  $\gamma_i$  as the closed orbit closest to the intersection curve  $\mathcal{S}(t_0) \cap \Pi_i$ .

Considering (12), we first observe that at each point  $x_0 \in \mathcal{M}_{\Delta}(t_0)$ , we would need to have  $\mathcal{M}_{\Delta}(t_0) \parallel \xi_2$ . Now consider that, in an initial reference plane  $\Pi_1$ , we have computed a curve  $\gamma_1$  as a closed orbit of  $\eta_{\delta,1}^{\pm}$ . Away from points with repeated eigenvalues of  $C_{t_0}^t$ , advecting  $\gamma_1$  under the  $\xi_2$ -field then yields a smooth tubular surface  $\mathcal{S}(t_0)$  that is tangent to  $\xi_2$ , just as  $\mathcal{M}_{\Delta}(t_0)$  should be. We then compute intersections of  $\mathcal{S}(t_0)$  with the remaining reference planes  $\Pi_{i=2,3,\dots}$ . In each reference plane  $\Pi_i$ , from the set of all available closed orbits of  $\eta_{\delta,i}^{\pm}$  (denoted by  $\Gamma_i$ ), select the orbit  $\gamma_i$  minimizing the min-distance to the intersection curve  $\mathcal{S}(t_0) \cap \Pi_i$ . That is, for each  $\tilde{\gamma} \in \Gamma_i$  evaluate

$$d(\tilde{\gamma}, \mathcal{S}(t_0) \cap \Pi_i) = \min_{q \in \tilde{\gamma}, p \in \mathcal{S}(t_0) \cap \Pi_i} \|q - p\|, \quad (15)$$

and take the orbit  $\tilde{\gamma}$  that minimizes the above expression as  $\gamma_i$ . At the end, interpolate the surface  $\mathcal{M}_{\Delta}(t_0)$  from the collection of closed orbits  $\gamma_i \parallel \eta_{\delta,i}^{\pm}$ .

The surface  $\mathcal{M}_{\Delta}(t_0)$  obtained from the above procedure (cf. Fig. 4) will generally not satisfy the helicity condition (14), because it will not be exactly tangent to  $\xi_2$ . The surface  $\mathcal{S}(t_0)$  is, however, tangent to  $\xi_2$ . In addition, locally,  $\mathcal{S}(t_0)$  has a smooth normal field of the general form  $\pm n_{\delta(x_0)}^{\pm}$  (see

(12)), and therefore satisfies a helicity condition of the type (14) (see Appendix F);  $\delta(x_0) \in [-1 + \frac{\lambda_1(x_0)}{\lambda_2(x_0)}, -1 + \frac{\lambda_3(x_0)}{\lambda_2(x_0)}]$  is unknown on  $\mathcal{S}(t_0)$  and possibly exceeds the range  $[-2\Delta + \Delta^2, 2\Delta + \Delta^2]$ . The above observations thus render the surface  $\mathcal{M}_{\Delta}(t_0)$  as close to a surface  $\mathcal{S}(t_0)$  that satisfies both tangency to  $\xi_2$  and a helicity condition of the intended functional form (14).

For the examples we study in Sec. VI, we find that it is not necessary to construct a full two-dimensional surface  $\mathcal{S}(t_0)$  by advecting the entire orbit  $\gamma_1$  under the  $\xi_2$ -field. It turns out that data points obtained from very few integral curves of  $\xi_2$ , launched from arbitrary points on  $\gamma_1$  (cf. Fig. 4), already lead to robust assessments of the min-distance (15). This discretization of  $\mathcal{S}(t_0)$  will therefore barely affect the selection of closed orbits  $\gamma_{2,3,\dots}$  for building a near-uniformly stretching material surface  $\mathcal{M}_{\Delta}(t_0)$ .

### C. Summary of the extraction procedure

Here, we briefly summarize the numerical extraction procedure for elliptic LCSs,  $\mathcal{M}_{\Delta}(t_0)$  (see Appendix G for details).

*Part 1* (computation of closed orbits): Sample the flow domain by defining a parallel stack of reference planes  $\Pi_i$ . For each reference plane  $\Pi_i$ , compute the Cauchy-Green strain tensor  $C_{t_0}^t$  on a square main grid. Using bilinear interpolation of the Cauchy-Green eigenvectors  $\xi_{1,2,3}$  and eigenvalues  $\lambda_{1,2,3}$ , compute closed integral curves of  $\eta_{\delta,i}^{\pm}$ , looping over both  $\sigma = +, -$  and  $\delta \in [-2\Delta + \Delta^2, 2\Delta + \Delta^2]$ .

*Part 2* (interpolation of closed orbits to an elliptic LCS surface): Consider the first reference plane  $\Pi_{i_0}$  containing at least one closed orbit of  $\eta_{\delta=0,i_0}^{\pm}$  in the region of interest. For visualizing the vortex boundary, pick the outermost closed orbit of  $\eta_{\delta=0,i_0}^{\pm}$ , denoted by  $\gamma_{i_0}$ . Starting from points on  $\gamma_{i_0}$ , integrate curves tangent to the  $\xi_2$ -line field ( $\xi_2$ -lines) until each reference plane containing closed orbits of  $\eta_{\delta,i}^{\pm}$  is intersected at least once. Iterate through the following reference planes  $\Pi_i$  ( $i = i_0 + 1, i_0 + 2, \dots$ ), and, in each, select the closed orbit of  $\eta_{\delta,i}^{\pm}$ , labeled  $\gamma_i$ , closest to the intersection points between  $\Pi_i$  and the  $\xi_2$ -line(s) (in the sense described in Sec. VB). At the end, use the data points given by the collection of closed orbits  $\{\gamma_i\}$  of the  $\eta_{\delta,i}^{\pm}$ -fields to interpolate a smooth surface  $\mathcal{M}_{\Delta}(t_0)$ .

## VI. EXAMPLES

### A. Steady ABC flow

We consider the steady ABC flow, a stationary solution of the Euler equations. In Cartesian coordinates  $(x, y, z)$ , its velocity field is given by

$$u(x, y, z) = \begin{pmatrix} A \sin(z) + C \cos(y) \\ B \sin(x) + A \cos(z) \\ C \sin(y) + B \cos(x) \end{pmatrix}, \quad (16)$$

where we select  $A = \sqrt{3}$ ,  $B = \sqrt{2}$ ,  $C = 1$ . For these parameter values, the ABC flow is known to contain several distinct vortical regions in the midst of a bulk of chaotic trajectories.<sup>4</sup> The flow domain is the three-torus  $\mathbb{T}^3$  or, equivalently, a

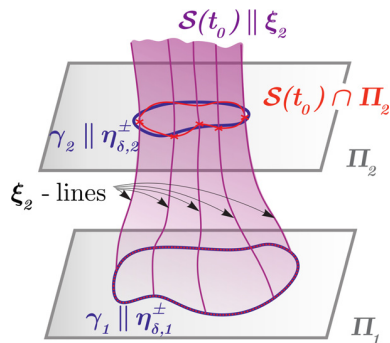


FIG. 4. Identifying the best candidate orbit of  $\eta_{\delta,2}^{\pm}$  in the  $\Pi_2$ -plane as the one with minimal distance to points of  $\mathcal{S}(t_0) \cap \Pi_2$ . Instead of computing the entire surface  $\mathcal{S}(t_0)$ , only few integral curves tangent to the  $\xi_2$ -field ( $\xi_2$ -lines) may already indicate a useful candidate orbit.

cube of  $[0, 2\pi]^3$  with periodic boundary conditions imposed on each face.

We sample the flow domain using a family of 100 uniformly spaced reference planes perpendicular to the  $z$ -axis, each of them given by

$$\Pi_i = \{(x, y, z) \in [0, 2\pi]^3 \mid z = (i - 1) \cdot 2\pi/100\},$$

$$i = 1, \dots, 100.$$

Choosing the extraction window as  $[t_0, t] = [0, 40]$ , we analyze the vortical region located around  $(x \approx 3.7, y \approx 4.7, z \approx 0.0)$ , seeking the largest elliptic LCS as a nearly uniformly stretching surface  $\mathcal{M}_\Delta(t_0)$  with pointwise relative stretching deviation up to  $\Delta = 0.1$  (see Appendix H for the remaining numerical details).

We scan the parameter window  $\delta \in [-0.19, 0.21]$  using 80 uniformly spaced  $\delta$ -values, and in addition run  $\delta = 0$  to identify closed orbits of  $\eta_{\delta,i}^\pm$  on all reference planes. In Fig. 5, we visualize part of the flow in lowest reference plane  $\Pi_1$  using the Finite-time Lyapunov Exponent (FTLE) field  $[2(t - t_0)]^{-1} \log \lambda_3$  and superimpose the closed orbits of  $\eta_{\delta,1}^\pm$ . The procedure described in part 2 of Appendix G then leads us to building the outermost elliptic LCS starting from the orbit  $\gamma_1$  indicated in Fig. 5. For the selection of the remaining closed orbits  $\gamma_{2,\dots,100}$ , we integrate one trajectory of  $\xi_2$  from  $(x \approx 4.34, y \approx 4.19, z = 0.0) \in \gamma_1$  to  $(x \approx 3.17, y \approx 5.11, z \approx 6.22) \in \Pi_{100}$ . We show the arclength and  $\delta$ -value of each orbit  $\gamma_{1,\dots,100}$  in Figs. 6(a) and 6(b). These provide qualitative insight into smoothness and stretching variation of the tubular surface  $\mathcal{M}_\Delta(t_0)$  that we then create from the orbits  $\gamma_{1,\dots,100}$  by interpolation. For better visualization of  $\mathcal{M}_\Delta(t_0)$ , we use toroidal coordinates  $(\bar{x}, \bar{y}, \bar{z})$

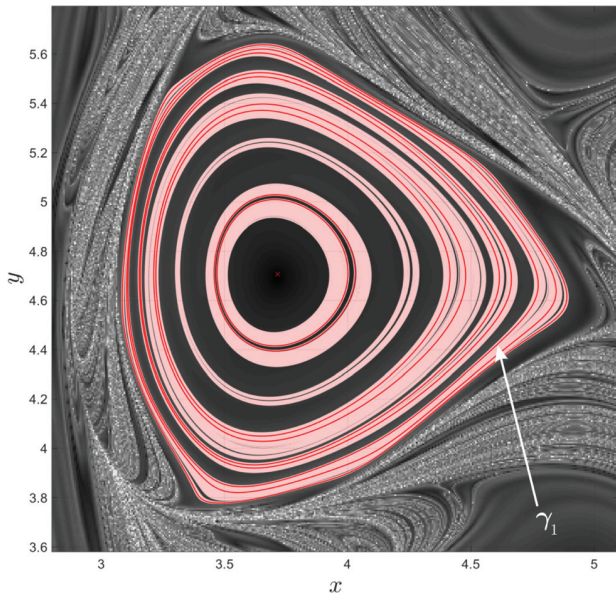


FIG. 5. Steady ABC flow, time-window  $[0, 40]$ : Closed orbits of  $\eta_{\delta,1}^\pm$  with  $\delta \in [-0.19, 0.21]$  in the plane  $\Pi_1$ , displaying curves with  $\delta = 0$  in strong red and with  $\delta \neq 0$  in light red. The red cross indicates the approximate vortex center. The curve  $\gamma_1$  is used as the initial orbit in the assembly of the elliptic LCS. Background visualization: Finite-time Lyapunov exponent field.

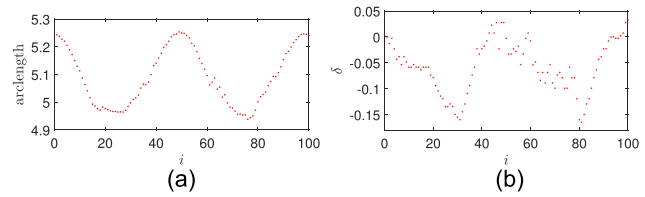


FIG. 6. Steady ABC flow, time-window  $[0, 40]$ : Properties of the closed orbits  $\gamma_{1,\dots,100}$  used to build an elliptic LCS. (a) Arclengths of the closed orbits  $\gamma_i$  selected on each reference plane. (b) Values of  $\delta$  of the closed orbits  $\gamma_i$  selected on each reference plane.

$$\bar{x} = (x - x_c(z) + R_1) \cos(z),$$

$$\bar{y} = (x - x_c(z) + R_1) \sin(z),$$

$$\bar{z} = R_2(y - y_c(z)),$$

with  $x_c(z), y_c(z)$  parametrizing the vortex center (extracted heuristically by local FTLE minima), and  $R_1 = 2, R_2 = 1$ . In Fig. 7(a), we show the final result for the elliptic LCS surface  $\mathcal{M}_\Delta(t_0)$  in red. We place a toroidal cloud of tracers closely around  $\mathcal{M}_\Delta(t_0)$  (purple dots), and then advect these together with  $\mathcal{M}_\Delta(t_0)$  over the time-window of extraction, as shown in Fig. 7(b). With the elliptic LCS at the final time  $\mathcal{M}_\Delta(t)$  displayed in green, we observe that  $\mathcal{M}_\Delta(t)$  preserves its coherence, while the purple tracer cloud disperses into a complex geometric structure.

For a longer extraction window  $[t_0, t] = [0, 250]$ , we also want to verify whether invariant tori of the steady ABC flow are well approximated by the elliptic LCSs we extract. In Fig. 8, we show a Poincaré map indicating all the invariant tori together with closed orbits of  $\eta_{\delta,1}^\pm$  in the  $\Pi_1$ -reference plane. Here, the relative stretching deviation we allow is again  $\Delta = 0.1$ , with the same sampling of  $\delta$ -values as above. Compared with Fig. 5, more closed orbits with  $\delta = 0$  are visible, indicating that there are more elliptic LCSs than for a shorter extraction time. As expected, the invariant tori are closely aligned with the elliptic LCSs. We show a representative elliptic LCS in Fig. 9.

### B. Time-a-periodic ABC-type flow

We consider a time-a-periodic modification of the ABC flow

$$u(x, y, z, \tau) = \begin{pmatrix} A_0 \sin(z) + (C_0 + C(\tau)) \cos(y) \\ (B_0 + B(\tau)) \sin(x) + A_0 \cos(z) \\ (C_0 + C(\tau)) \sin(y) + (B_0 + B(\tau)) \cos(x) \end{pmatrix},$$

(17)

with  $A_0 = \sqrt{3}, B_0 = \sqrt{2}$ , and  $C_0 = 1$ . The added time-dependent perturbations are

$$B(\tau) = B_0 k_0 \tanh(k_1 \tau) \cos((k_2 \tau)^2),$$

$$C(\tau) = C_0 k_0 \tanh(k_1 \tau) \sin((k_2 \tau)^2),$$

where  $k_0 = 0.15, k_1 = 0.05$ , and  $k_2 = 0.12$ . We plot  $B(\tau)$  and  $C(\tau)$  in Fig. 10. The time-dependence we have selected for these functions models how the steady ABC flow, a locally unstable solution to the Euler equations,<sup>10</sup> develops

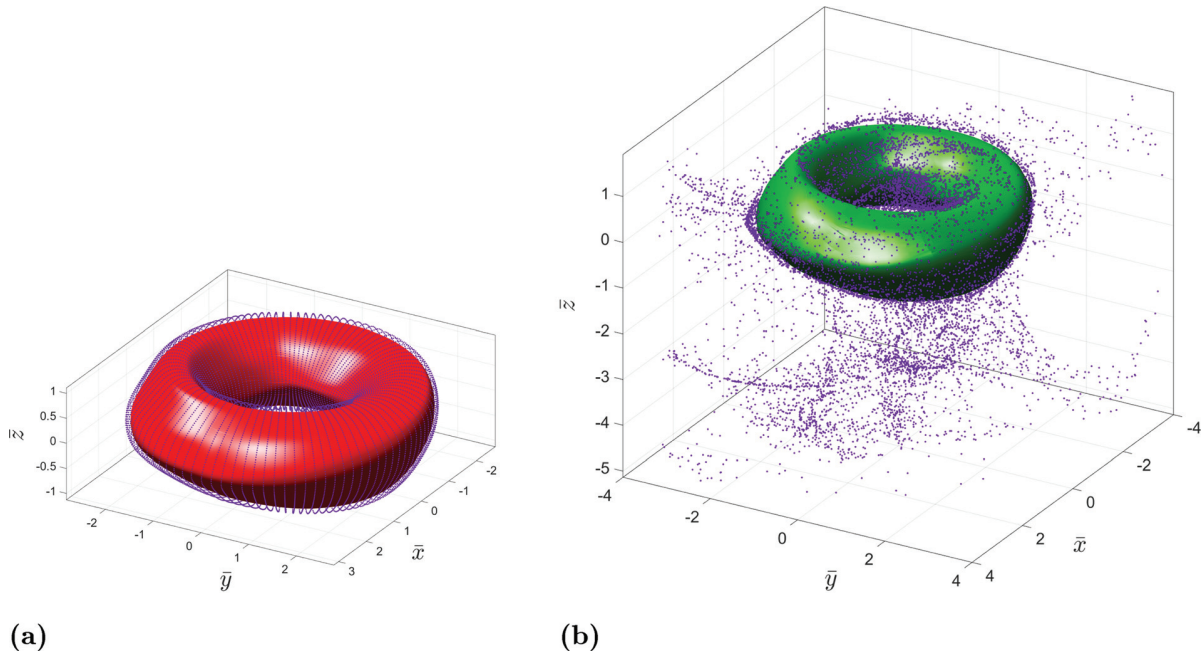


FIG. 7. Steady ABC flow, time-window [0, 40]: Advecting the elliptic LCS from  $t_0=0$  to  $t=40$ , in comparison to nearby tracers, which spread incoherently. (a) Red: elliptic LCS  $\mathcal{M}_{\Delta=0.1}(t_0=0)$ , extracted for the time-interval [0, 40]. Purple: locations of tracers placed closely outside the LCS surface. (b) Green: time-40 advected image of the elliptic LCS in Fig. 7(a). Purple: tracers advected from the locations in Fig. 7(a).

oscillations followed by saturation into another ABC-type flow with aperiodic time-dependence.

Like for the steady ABC flow, we consider the time-interval [0, 40] and analyze the vortical region located around  $(x \approx 3.7, y \approx 4.7, z \approx 0.0)$ . We allow a pointwise stretching variation  $\Delta=0.15$  for constructing the barrier, sampling the interval of  $\delta \in [-0.2775, 0.3225]$  with 160 uniformly spaced values and, in addition,  $\delta=0$  (see Appendix

H for the remaining numerical details). We show the closed orbits of  $\eta_{\delta,1}^{\pm}$  in the lowest reference plane  $\Pi_1$  at  $z=0$  in Fig. 11. The integral curve of  $\zeta_2$  used for the selection of the remaining closed orbits  $\gamma_{2,\dots,100}$  connects  $(x \approx 3.64, y \approx 4.15, z=0.0) \in \gamma_1$  and  $(x \approx 3.32, y \approx 4.88, z \approx 6.22) \in \Pi_{100}$ . The arclengths and  $\delta$ -values of these orbits  $\gamma_{1,\dots,100}$  constituting the LCS  $\mathcal{M}_{\Delta}(t_0)$  are shown in Figs. 12(a) and 12(b).

For  $t_0=0$ , we visualize this largest elliptic LCS  $\mathcal{M}_{\Delta}(t_0)$  as the red surface in Fig. 13(a), together with purple dots indicating a toroidal cloud of tracers placed closely around it. In comparison to the green surface  $\mathcal{M}_{\Delta}(t)$  in Fig. 13(b), we see that the elliptic LCS  $\mathcal{M}_{\Delta}(\tau)$  does move under advection over [0, 40], but keeps its coherence. The purple tracer cloud, on the other hand, starts to develop two filaments.

Comparing Fig. 13(b) to Fig. 7(b), we see that the steady ABC flow spreads tracers outside the elliptic LCS more than

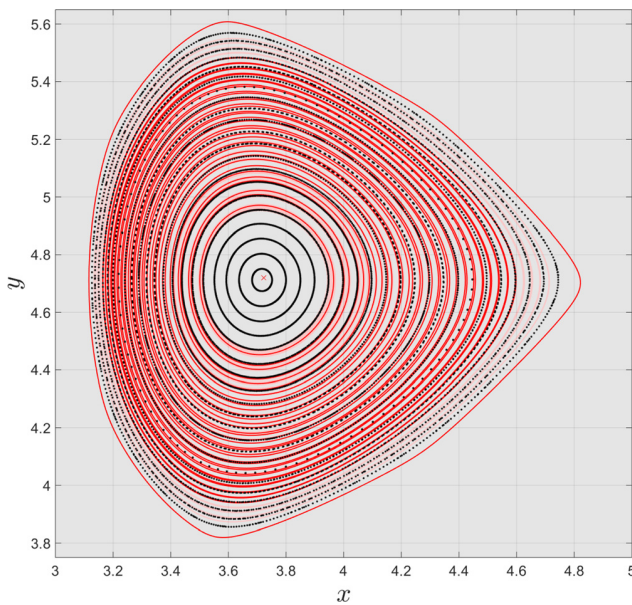


FIG. 8. Steady ABC flow, time-window [0, 250]: Closed orbits of  $\eta_{\delta,1}^{\pm}$  with  $\delta \in [-0.19, 0.21]$  in the plane  $\Pi_1$ , displaying curves with  $\delta=0$  in strong red and with  $\delta \neq 0$  in light red. The red cross indicates the approximate vortex center. Black: Poincaré map obtained from the long-time behavior of multiple trajectories of (16).

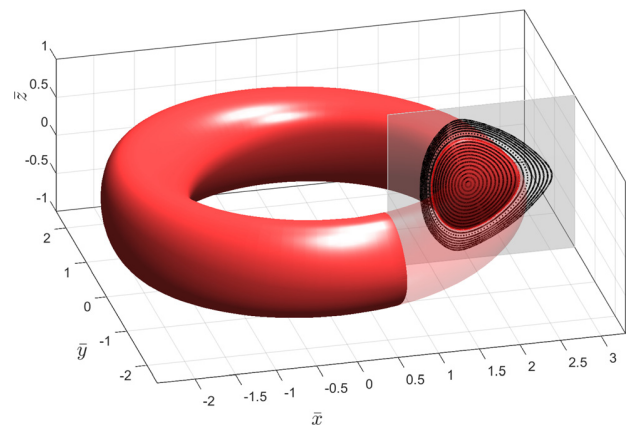


FIG. 9. Steady ABC flow, time-window [0, 250]: Representative 3D elliptic LCS and Poincaré map from Fig. 8.

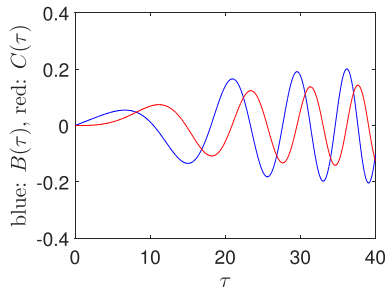


FIG. 10. Time-dependence of the coefficients of the unsteady ABC-type flow (17).

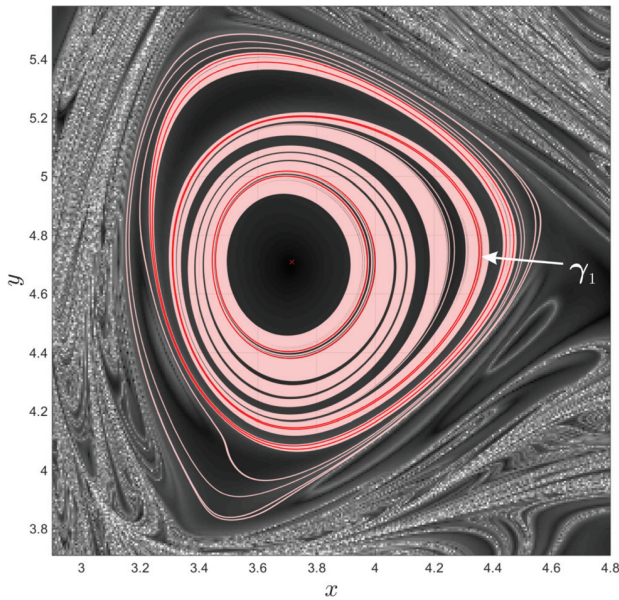
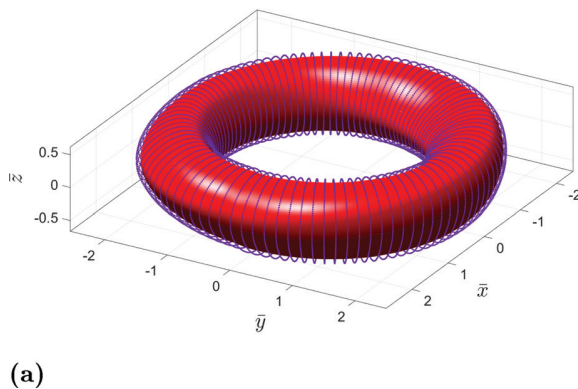


FIG. 11. Aperiodic ABC-type flow, time-window [0, 40]: Closed orbits of  $\eta_{\delta,1}^+$  with  $\delta \in [-0.2775, 0.3225]$  in the plane  $\Pi_1$ , displaying curves with  $\delta = 0$  in strong red and with  $\delta \neq 0$  in light red. The red cross indicates the approximate vortex center. The curve  $\gamma_1$  is used as the initial orbit in the assembly of the elliptic LCS. Background visualization: Finite-time Lyapunov exponent field.



(a)

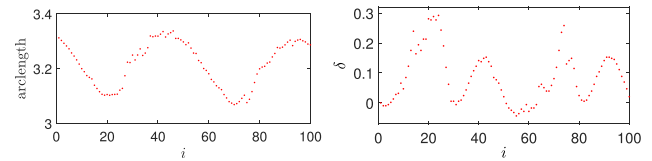


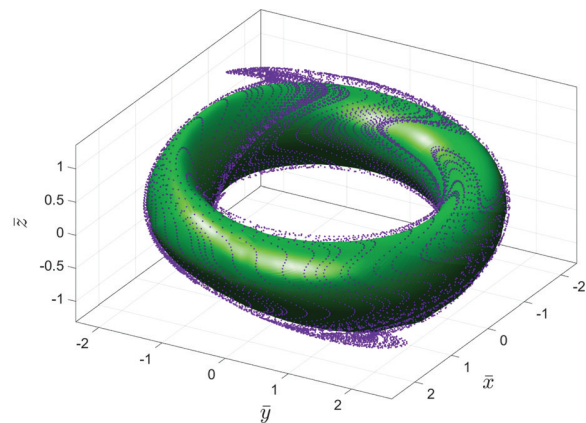
FIG. 12. Aperiodic ABC-type flow, time-window [0, 40]: Properties of the closed orbits  $\gamma_1, \dots, \gamma_{100}$  used to build an elliptic LCS. (a) Arclengths of the closed orbits  $\gamma_i$  selected on each reference plane. (b) Values of  $\delta$  of the closed orbits  $\gamma_i$  selected on each reference plane.

the time-aperiodic version. This phenomenon arises as follows: The LCS we obtain for the steady ABC flow is the outermost structure of a large family of nested tori that are going to advect coherently. Parts of the tracer cloud placed around the LCS are already in the chaotic region and undergo large stretching. Including time-aperiodic functions in the coefficients of the ABC flow, on the other hand, lets a large number of the outermost tori disappear. Consequently, the LCS we obtain in the aperiodic case is much smaller and far away from the hyperbolic structures. In comparison to the steady case, tracers initialized along the LCS we obtain in the time-aperiodic ABC type flow thus experience less dramatic stretching over the time interval considered here.

The vortices in the two ABC-type flows analyzed here have a simpler spatial structure than the ones analyzed in other works (e.g., Ref. 28). Here, our focus is to describe a new method and provide a proof of concept in a simpler setting. Analyzing a time-aperiodic version of the time-periodic flow considered in Ref. 28 would be a worthwhile application of the approach derived here.

### VII. CONCLUSIONS

We have extended the construction of elliptic LCSs as uniformly stretching material surfaces from the two-dimensional setting of Ref. 17 to three-dimensional unsteady flows. With this approach, we obtain near-uniformly stretching tubular material surfaces that do not filament under the flow. This is in contrast to the 3D elliptic LCS approach



(b)

FIG. 13. Aperiodic ABC-type flow, time-window [0, 40]: Advecting the elliptic LCS from  $t_0 = 0$  to  $t = 40$ , in comparison to tracers. (a) Red: elliptic LCS  $\mathcal{M}_{\Delta=0.1}(t_0 = 0)$ , extracted for the time-interval [0, 40]. Purple: locations of tracers placed closely outside the LCS surface. (b) Green: time-40 advected image of the elliptic LCS in Fig. 13(a). Purple: tracers advected from the locations in Fig. 13(a).

from Ref. 2, which imposes a strict point-wise maximum shear principle. For the steady ABC flow, we have shown that our elliptic LCS construction identifies invariant tori revealed also by the Poincaré map. In an aperiodically driven ABC-type flow, we have located temporally aperiodic non-filamenting tori. The two-dimensional version<sup>17</sup> of the present ideas has proven effective in locating material boundaries of Agulhas rings in the South Atlantic,<sup>17,31</sup> of the Great Red Spot of Jupiter,<sup>13</sup> and of coherent Lagrangian vortices in the wake of swimming fish.<sup>19</sup> Our method offers a similar tool for locating coherent material vortex boundaries in three-dimensional numerical and experimental, highly resolved velocity data.

Recent work<sup>18</sup> has identified rotationally coherent (and not necessarily uniformly stretching) LCSs using the Lagrangian-Averaged Vorticity Deviation (LAVD). This approach, therefore, targets flows with non-vanishing vorticity. The present approach makes no such assumption and hence is of general relevance for 3D dynamical systems that are not necessarily fluid flows.

Another recent approach identifies elliptic LCSs in two- and three-dimensional flows from tubular level sets of the polar rotation angle (PRA).<sup>9</sup> The PRA measures the total rotation of the Cauchy-Green eigenbasis under the deformation gradient. The PRA is obtained from the polar decomposition of the deformation gradient into a rotation tensor and a right stretch tensor. The latter has the same eigenvalues and eigenvectors as the Cauchy-Green strain tensor and thus contains all the quantities needed to define the surfaces we use here (cf. Definition 2). Defining the PRA, on the other hand, requires the rotation tensor only. The PRA approach can hence be viewed as dual to the present method and is applicable beyond fluid flows as well. In contrast to extracting near-uniformly stretching surfaces, however, identifying structures from PRA level sets is not an objective (frame-invariant) method in three-dimensional flows. The present approach overcomes this limitation.

**ACKNOWLEDGMENTS**

We thank Alireza Hadjighasem and Daniel Karrasch for helpful discussions and suggestions.

**APPENDIX A: DETAILS ON SOLVING (8) IN THE PROOF OF THEOREM 1**

We examine why the solution set of (8) in the case of  $\lambda = \sqrt{\lambda_2}$  consists of two planes, while  $\lambda = \sqrt{\lambda_3}$  and  $\lambda = \sqrt{\lambda_1}$  yield lines.

For  $\lambda = \sqrt{\lambda_2}$ , (8) can be written as

$$\alpha^2(\lambda_2 - \lambda_1) + \gamma^2(\lambda_2 - \lambda_3) = 0. \tag{A1}$$

Rearranging this equation, we obtain

$$\gamma = \mp \sqrt{\frac{\lambda_2 - \lambda_1}{\lambda_3 - \lambda_2}} \alpha.$$

The solution set of (8) for  $\lambda = \sqrt{\lambda_2}$  is therefore given by two planes. (These planes are normal to the unit vectors  $n^\pm$  defined in (9).)

For  $\lambda = \sqrt{\lambda_3}$ , (8) can be written as

$$\alpha^2(\lambda_3 - \lambda_1) + \beta^2(\lambda_3 - \lambda_2) = 0. \tag{A2}$$

This equation is similar to (A1), but, since both  $(\lambda_3 - \lambda_1) > 0$  and  $(\lambda_3 - \lambda_2) > 0$ , the only solution of (A2) is given by  $\alpha = \beta = 0$ ,  $\gamma \in \mathbb{R}$  (which is exactly the  $\xi_3$ -axis). For  $\lambda = \sqrt{\lambda_1}$ , we similarly conclude that the  $\xi_1$ -axis is the solution set of (8).

The reasoning leading to double cones for the remaining two cases of  $\lambda \in (\lambda_1, \lambda_2)$  and  $\lambda \in (\lambda_2, \lambda_3)$  will appear in Appendix C. We hence omit it here for brevity.

**APPENDIX B: REPEATED EIGENVALUES IN THE PROOF OF THEOREM 1**

Given the initial position  $\mathcal{M}(t_0)$  of a pointwise uniformly stretching material surface  $\mathcal{M}(\tau)$ , we show that  $\lambda(x_0) = \sqrt{\lambda_2(x_0)}$  holds for all points  $x_0 \in \mathcal{M}(t_0)$  where the Cauchy-Green strain tensor has repeated eigenvalues:

- For any point  $x_0 \in \mathcal{M}(t_0)$  where  $\lambda_1(x_0) \neq \lambda_2(x_0) = \lambda_3(x_0)$ , we may repeat the procedure as for points with distinct eigenvalues. For the expansion of  $v \in T_{x_0}\mathcal{M}(t_0)$ , pick any two orthogonal vectors  $\tilde{\xi}_{2,3}$  in the plane normal to  $\xi_1(x_0)$ , and write  $v = \alpha\tilde{\xi}_1 + \beta\tilde{\xi}_2 + \gamma\tilde{\xi}_3$ . The  $\lambda$ -stretching condition is then identical to (8) with  $\lambda_2 = \lambda_3$ , that is

$$\alpha^2(\lambda^2 - \lambda_1) + (\beta^2 + \gamma^2)(\lambda^2 - \lambda_2) = 0. \tag{B1}$$

Here, three cases are possible: If  $\lambda = \sqrt{\lambda_1}$ , then the solution set of (B1) is the  $\xi_1$ -axis (see case 1 in Table I). If  $\lambda \in (\sqrt{\lambda_1}, \sqrt{\lambda_2})$ , then the solution set of (B1) is a circular double cone about the  $\xi_1$ -axis (see case 2 in Table I). If  $\lambda = \sqrt{\lambda_2}$ , then directions satisfying (B1) form a plane perpendicular to  $\xi_1$ . (This corresponds to case 3 in Table I, with the two planes collapsed into one.) This implies that the tangent plane  $T_{x_0}\mathcal{M}(t_0)$  is normal to  $\xi_1(x_0)$ . Vectors tangent to  $\mathcal{M}(t_0)$  therefore stretch by  $\lambda(x_0) = \sqrt{\lambda_2(x_0)} = \sqrt{\lambda_3(x_0)}$ .

- For any point  $x_0 \in \mathcal{M}(t_0)$  where  $\lambda_1(x_0) = \lambda_2(x_0) \neq \lambda_3(x_0)$ , repeating the argument from above shows that there exists a plane of uniformly stretching directions perpendicular to  $\xi_3(x_0)$ . With the tangent plane  $T_{x_0}\mathcal{M}(t_0)$  therefore being perpendicular to  $\xi_3(x_0)$ , we conclude that all vectors from  $T_{x_0}\mathcal{M}(t_0)$  stretch by  $\lambda(x_0) = \sqrt{\lambda_1(x_0)} = \sqrt{\lambda_2(x_0)}$ .
- For any point  $x_0 \in \mathcal{M}(t_0)$  where  $\lambda_1(x_0) = \lambda_2(x_0) = \lambda_3(x_0)$ , the surface  $\mathcal{M}(t_0)$  may be perpendicular to any unit normal  $n(x_0) \in S^2$ . All elements of its tangent space  $T_{x_0}\mathcal{M}(t_0)$  then stretch by  $\lambda(x_0) = \sqrt{\lambda_1(x_0)} = \sqrt{\lambda_2(x_0)} = \sqrt{\lambda_3(x_0)}$ .

**APPENDIX C: GEOMETRY OF ELLIPTIC CONES AND PLANES**

In order to motivate the expression for  $n_\delta^\pm(x_0)$  given in (12), consider  $\lambda^2(x_0) = \lambda_2(x_0)(1 + \delta)$  with positive  $\delta \in (0, -1 + \frac{\lambda_3(x_0)}{\lambda_2(x_0)})$  (case 4 in Table I), and examine Equation (8) of  $\lambda$ -stretching directions. After rearranging and again omitting the position arguments, we find

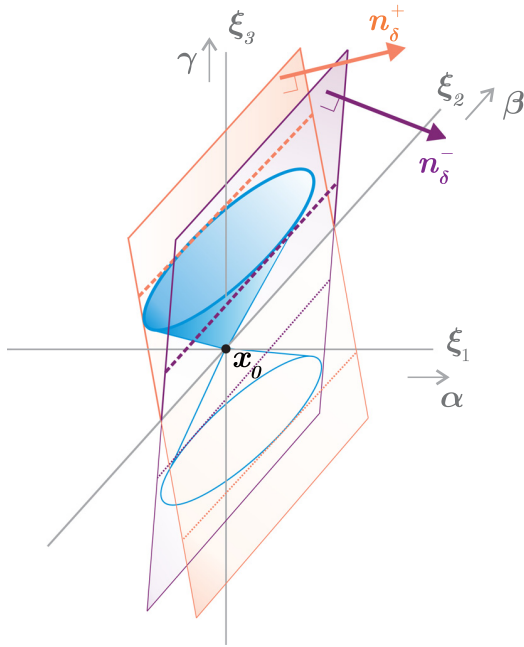


FIG. 14. Small  $\delta > 0$ : The elliptic double cones of  $\lambda$ -stretching directions can be approximated by a pair of planes.

$$\frac{\alpha^2}{a^2} + \frac{\beta^2}{b^2} = 1, \tag{C1}$$

where

$$a = \sqrt{\frac{\lambda_3 - \lambda_2(1 + \delta)}{\lambda_2(1 + \delta) - \lambda_1}} \gamma^2, \quad b = \sqrt{\frac{\lambda_3 - \lambda_2(1 + \delta)}{\lambda_2 \delta}} \gamma^2.$$

For any fixed  $\gamma$ , and recalling that  $\alpha, \beta, \gamma$  are the coordinates along  $\xi_1, \xi_2, \xi_3$ , we recognize (C1) as the equation of an ellipse with minor axis  $\xi_1$  and major axis  $\xi_2$ . This explicitly shows that the  $\lambda$ -stretching directions form elliptic double cones about the  $\xi_3$ -axis (Table I). Considering small  $\delta$ , we have that  $b \gg a$ , confirming that these cones are indeed elongated along the  $\xi_2$ -axis. We therefore approximate these cones using the two planes shown in purple and orange in Fig. 14. Setting  $\beta = 0$  in (C1), we find that such cones satisfy

$$\gamma = \mp \sqrt{\frac{\lambda_2(1 + \delta) - \lambda_1}{\lambda_3 - \lambda_2(1 + \delta)}} \alpha,$$

and hence the two planes are perpendicular to the unit vectors  $n_\delta^\pm$  given in (12). We omit repeating the argument for  $\delta < 0$ .

#### APPENDIX D: ANGLE PRESERVATION WITHIN UNIFORMLY STRETCHING SURFACES

As shown in Appendix A, at any initial position  $x_0$ , a uniformly stretching surface  $\mathcal{M}(t_0)$  will be perpendicular to one of the two possible unit normals

$$n_0^\pm(x_0) = n_{\delta=0}^\pm(x_0) = \sqrt{\frac{\lambda_2(x_0) - \lambda_1(x_0)}{\lambda_3(x_0) - \lambda_1(x_0)}} \xi_1(x_0) \pm \sqrt{\frac{\lambda_3(x_0) - \lambda_2(x_0)}{\lambda_3(x_0) - \lambda_1(x_0)}} \xi_3(x_0). \tag{D1}$$

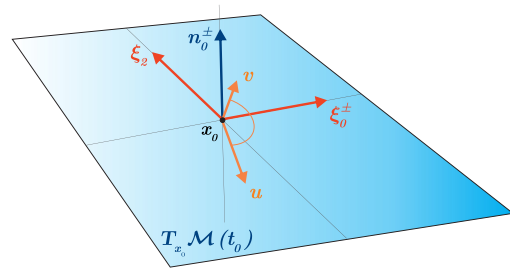


FIG. 15. Set-up to evaluate the change of angle between two arbitrary-vectors  $u, v \in T_{x_0} \mathcal{M}(t_0)$  under advection by  $DF_{t_0}^t$ .

The tangent space  $T_{x_0} \mathcal{M}(t_0)$  is therefore spanned by  $\xi_2(x_0)$  and

$$\xi_0^\pm(x_0) := \pm \sqrt{\frac{\lambda_3(x_0) - \lambda_2(x_0)}{\lambda_3(x_0) - \lambda_1(x_0)}} \xi_1(x_0) - \sqrt{\frac{\lambda_2(x_0) - \lambda_1(x_0)}{\lambda_3(x_0) - \lambda_1(x_0)}} \xi_3(x_0). \tag{D2}$$

With these definitions, we have  $\xi_0^\pm(x_0) \times \xi_2(x_0) = n_0^\pm(x_0)$ . Consider two arbitrary vectors  $u, v \in T_{x_0} \mathcal{M}(t_0)$ , see Fig. 15. We expand them in the orthonormal basis defined above, dropping the position label

$$u = u_0 \xi_0^\pm + u_2 \xi_2, \\ v = v_0 \xi_0^\pm + v_2 \xi_2.$$

By the singular-value decomposition of  $DF_{t_0}^t$  (cf. Ref. 20), one obtains that under advection from time  $t_0$  to time  $t$ , the eigenvectors of  $C_{t_0}^t$  are mapped according to

$$DF_{t_0}^t \xi_i = \sqrt{\lambda_i} \theta_i, \quad i = 1, 2, 3, \tag{D3}$$

where  $\theta_{1,2,3}$  are orthonormal eigenvectors of the left Cauchy-Green strain tensor  $B_{t_0}^t = DF_{t_0}^t (DF_{t_0}^t)^T$ . Applying these relations after fully writing out  $u$  and  $v$  in terms of the  $\xi_i$ -vectors, we obtain

$$\langle DF_{t_0}^t u, DF_{t_0}^t v \rangle = \lambda_2(u_0 v_0 + u_2 v_2) \equiv \lambda_2 \langle u, v \rangle, \\ \|DF_{t_0}^t u\| = \sqrt{\lambda_2} \sqrt{(u_0)^2 + (u_2)^2} = \sqrt{\lambda_2} \|u\|, \\ \|DF_{t_0}^t v\| = \sqrt{\lambda_2} \|v\|.$$

Combining these expressions yields

$$\frac{\langle DF_{t_0}^t u, DF_{t_0}^t v \rangle}{\|DF_{t_0}^t u\| \cdot \|DF_{t_0}^t v\|} = \frac{\langle u, v \rangle}{\|u\| \cdot \|v\|}, \tag{D4}$$

which means that, under advection from time  $t_0$  to time  $t$ , the angle between  $u, v$  is indeed preserved.

#### APPENDIX E: PROOF OF PROPOSITION 1

Consider an arbitrary unit normal  $n \in S^2$  and the plane  $\Pi_n$  perpendicular to it,  $\Pi_n = \{v \in \mathbb{R}^3 | \langle v, n \rangle = 0\}$ . We introduce an orthonormal basis  $ijk$  of  $\mathbb{R}^3$  such that  $i$  and  $j$  lie in  $\Pi_n$  and  $k: = i \times j \equiv n$ . We parametrize directions  $\eta \in S^2 \cap \Pi_n$  by

$$\eta = \eta(\phi) = i \cos(\phi) + j \sin(\phi), \quad \phi \in [0, 2\pi). \tag{E1}$$

The stretching within  $\Pi_n$  can then be mapped out by introducing a function

$$q_n(\phi) := \sqrt{\langle \eta(\phi), C'_{i_0} \eta(\phi) \rangle}. \tag{E2}$$

(See Fig. 16 for an illustration of the set-up.) We evaluate (E2) explicitly in terms of the Cauchy-Green invariants.

$$q_n(\phi) = \begin{cases} \sqrt{\frac{\lambda_1(n_3 \cos \phi - n_1 n_2 \sin \phi)^2 + \lambda_2(n_1^2 + n_3^2) \sin^2 \phi + \lambda_3(n_1 \cos \phi + n_2 n_3 \sin \phi)^2}{n_1^2 + n_3^2}}, & \text{if } n \neq \pm \xi_2, \\ \sqrt{\lambda_3 + (\lambda_1 - \lambda_3) \cos^2(\phi)}, & \text{if } n = \pm \xi_2. \end{cases} \tag{E3}$$

In particular

$$q_{\pm n_\delta^\pm}(\phi) = \sqrt{\lambda_2(1 + \delta \cos^2 \phi)}, \tag{E4}$$

$$q_{\pm \xi_1}(\phi) = \sqrt{\lambda_2 + (\lambda_3 - \lambda_2) \cos^2(\phi)}, \tag{E5}$$

$$q_{\pm \xi_3}(\phi) = \sqrt{\lambda_2 + (\lambda_1 - \lambda_2) \cos^2(\phi)}. \tag{E6}$$

*Proof.* If  $n \neq \pm \xi_2$ , writing out the equations  $\langle i, n \rangle = 0$  and  $\langle i, \xi_2 \rangle = 0$  while requiring  $i \in S^2$  allows two coordinate expressions for  $i$  with opposite orientation, from which we pick

$$i = \frac{n_3}{\sqrt{n_1^2 + n_3^2}} \xi_1 - \frac{n_1}{\sqrt{n_1^2 + n_3^2}} \xi_3.$$

From  $j = k \times i = n \times i$ , we get that

$$j = -\frac{n_1 n_2}{\sqrt{n_1^2 + n_3^2}} \xi_1 + \sqrt{n_1^2 + n_3^2} \xi_2 - \frac{n_2 n_3}{\sqrt{n_1^2 + n_3^2}} \xi_3.$$

Plugging these expressions into (E1) and then (E2) yields the first equation in (E3).  $\square$

*Proof.* [of Proposition 1] For any given  $\lambda$ , first consider  $n = \pm n_\delta^\pm$  with  $\delta = \lambda^2/\lambda_2 - 1$ . Equation (E4) shows that the range of stretching values attained in  $\Pi_{\pm n_\delta^\pm}$  is the interval

$$[\min\{\lambda, \sqrt{\lambda_2}\}, \max\{\lambda, \sqrt{\lambda_2}\}]. \tag{E7}$$

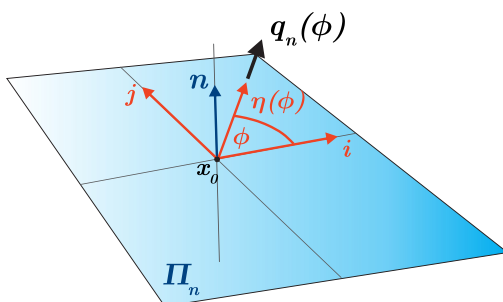


FIG. 16. Mapping out the stretching within  $\Pi_n$ , see also (E1) and (E2).

**Lemma 1.** Using the above definitions, choosing

$$\begin{cases} \langle i, \xi_2 \rangle = 0, & \text{sgn}(\langle i, \xi_1 \rangle) = \text{sgn}(n_3) & \text{if } n \neq \pm \xi_2, \\ i = \xi_1, & j = -\xi_3 & \text{if } n = \pm \xi_2, \end{cases}$$

and expanding  $n = n_1 \xi_1 + n_2 \xi_2 + n_3 \xi_3$ , we find

We compare this to what an arbitrary  $n \in S^2$  can provide for any prescribed  $\lambda$ : If  $\lambda > \lambda_2$ , consider that  $\Pi_n \cap \Pi_{\xi_3} \neq \emptyset$  always holds, and thus by Eq. (E6) there exists a  $\phi_0$  such that  $q_n(\phi_0) \in [\sqrt{\lambda_1}, \sqrt{\lambda_2}]$ . The smallest range of stretching values within  $\Pi_n$  that one could possibly obtain is therefore  $[\sqrt{\lambda_2}, \lambda]$ . But this is exactly what we have already achieved above by taking  $n = \pm n_\delta^\pm$ , see (E7), rendering it the optimal choice. If  $\lambda < \sqrt{\lambda_2}$ , repeat the argument considering  $\Pi_n \cap \Pi_{\xi_1} \neq \emptyset$ , which by Eq. (E5) means that there exists a  $\phi_0$  such that  $q_n(\phi_0) \in [\sqrt{\lambda_2}, \sqrt{\lambda_3}]$ , and therefore the smallest possible range is  $[\lambda, \sqrt{\lambda_2}]$ . This can again be achieved with  $n = \pm n_\delta^\pm$ .  $\square$

**APPENDIX F: CONNECTION BETWEEN SURFACES TANGENT TO  $\xi_2$  AND THE  $n_\delta^\pm$  FIELDS**

We consider an arbitrary smooth surface tangent to  $\xi_2$  and relate its normal field to the normal fields  $\pm n_\delta^\pm$  (see (12), taking into account orientation here).

**Lemma 2.** Consider a surface  $S(t_0)$  that is normal to the vector field

$$m_\phi = \cos \phi \xi_1 + \sin \phi \xi_3, \tag{F1}$$

with  $\phi : x_0 \mapsto \phi(x_0) \in [0, 2\pi)$  denoting a scalar field on  $S(t_0)$ . Then for each  $x_0 \in S(t_0)$ , there exists an injective function  $F$  from  $\phi$  to  $(\delta, \sigma_1, \sigma_2)$ , the parameters of the vector field  $n_\delta^{\sigma_1, \sigma_2}$ . Here,  $n_\delta^{\sigma_1, \sigma_2}$  is related to  $n_\delta^\pm$  (12) via  $n_\delta^{\sigma_1, \sigma_2} = \sigma_2 n_\delta^{\sigma_1}$ , i.e., we define

$$n_\delta^{\sigma_1, \sigma_2} = \sigma_2(a_\delta \xi_1 + \sigma_1 c_\delta \xi_3), \quad a_\delta = \sqrt{\frac{\lambda_2(1 + \delta) - \lambda_1}{\lambda_3 - \lambda_1}},$$

$$c_\delta = \sqrt{\frac{\lambda_3 - \lambda_2(1 + \delta)}{\lambda_3 - \lambda_1}}, \quad \sigma_{1,2} \in \{-1, 1\}.$$

*Proof.* Solving either  $a_\delta = \cos \phi$  or  $c_\delta = \sin \phi$  for  $\delta$  yields

$$\delta = f(\phi) := \frac{\lambda_1 - \lambda_2 + (\lambda_3 - \lambda_1) \cos^2 \phi}{\lambda_2}.$$

We thus define the function  $F$  as

$$F : \begin{cases} [0, \pi) & \rightarrow \left[-1 + \frac{\lambda_1}{\lambda_2}, -1 + \frac{\lambda_3}{\lambda_2}\right] \times \{-1, 1\} \times \{-1, 1\}, \\ \phi & \mapsto (F_0(\phi), F_1(\phi), F_2(\phi)) := \begin{cases} (f(\phi), 1, 1), & \text{if } \phi \in [0, \pi/2), \\ (f(\phi), -1, 1) & \text{if } \phi \in [\pi/2, \pi), \\ (f(\phi), 1, -1) & \text{if } \phi \in [\pi, 3\pi/2), \\ (f(\phi), -1, -1) & \text{if } \phi \in [3\pi/2, 2\pi). \end{cases} \end{cases} \quad \square$$

Now consider an arbitrary smooth surface  $\mathcal{S}(t_0)$  tangent to  $\xi_2$ . Since  $\mathcal{S}(t_0)$  does not contain points where  $C'_{t_0}$  has repeated eigenvalues, locally, the direction fields  $\xi_1$  and  $\xi_3$  can be oriented into smooth vector fields. The normal field of  $\mathcal{S}(t_0)$  is therefore given by a smooth vector field  $m_\phi$  of the form (F1). Allowing  $\delta \in \left[-1 + \frac{\lambda_1}{\lambda_2}, -1 + \frac{\lambda_3}{\lambda_2}\right]$  to vary in space, we choose  $(\delta, \sigma_1, \sigma_2) = (F_0(\phi), F_1(\phi), F_2(\phi))$  and identify

$$m_\phi = n_{F_0(\phi)}^{F_1(\phi), F_2(\phi)} = n_\delta^{\sigma_1, \sigma_2} = \sigma_2 n_\delta^{\sigma_1}.$$

The surface  $\mathcal{S}(t_0)$  therefore satisfies the helicity condition

$$\langle \nabla \times m_\phi, m_\phi \rangle = \langle \nabla \times n_\delta^{\sigma_1}, n_\delta^{\sigma_1} \rangle = 0.$$

### APPENDIX G: DETAILED SUMMARY OF THE EXTRACTION PROCEDURE

Here, we summarize the numerical extraction procedure for elliptic LCSs,  $\mathcal{M}_\Delta(t_0)$ , in detail:

*Part 1:* Using a parallel stack of square grids, each of them corresponding to one reference plane  $\Pi_i$ , define a 3D main grid in the flow domain. For each reference plane  $\Pi_i$ , compute closed orbits of  $\eta_{\delta,i}^\pm$ . The steps listed below are similar to the procedure for (elliptic) LCS computations in two dimensions:<sup>8,17</sup>

- (1) Compute an approximation to the Cauchy-Green strain tensor  $C'_{t_0}$ : Along each of the three coordinate axes defined by the 3D Cartesian grid, place two particles with displacements  $-d$  and  $+d$  relative to each main grid point of the current reference plane. Obtain their flow maps by integration of the velocity field. Using finite-differencing,<sup>16</sup> approximate  $DF'_{t_0}$  and thus  $C'_{t_0}$ .
- (2) Use an eigensolver to compute the Cauchy-Green invariants  $\xi_{1,2,3}$  and  $\lambda_{1,2,3}$  on each main grid point.
- (3) Using bilinear interpolation for  $\lambda_{1,2,3}$  and the components of  $\xi_{1,2,3}$ , compute closed integral curves of  $\eta_{\delta,i}^\sigma$ , looping over both  $\sigma = +, -$  and  $\delta \in [-2\Delta + \Delta^2, 2\Delta + \Delta^2]$ . This is easiest to do using a one-dimensional Poincaré section within  $\Pi_i$  as a secondary one-dimensional grid of initial conditions for candidate orbits of  $\eta_{\delta,i}^\sigma$ . We then detect closed orbits of  $\eta_{\delta,i}^\sigma$  from changes in the spiralling behaviour of the candidate orbits, refining the result by the bisection method.

*Part 2:* Select closed orbits  $\{\gamma_i\}$  and interpolate to obtain an elliptic LCS surface  $\mathcal{M}_\Delta(t_0)$ :

- (1) Consider the first reference plane  $\Pi_{i_0}$  containing at least one closed orbit of  $\eta_{\delta=0,i_0}^\pm$  in the region of interest. For the purpose of visualizing the vortex boundary, we pick the outermost closed orbit, which we refer to as  $\gamma_{i_0}$ .
- (2) Construct (parts of)  $\mathcal{S}(t_0)$ : Starting from points on  $\gamma_{i_0}$ , integrate curves tangent to the  $\xi_2$ -line field ( $\xi_2$ -lines) until each reference plane containing closed orbits of  $\eta_{\delta,i}^\pm$  is intersected at least once. When integrating  $\xi_2$ -lines, for each integration step, we recompute  $\xi_2$  by placing 6 particles at distances  $\pm d$  from the current point of the trajectory (see part 1, steps 1 and 2).
- (3) In the following reference plane  $\Pi_{i_0+1}$ , select the closed orbit of  $\eta_{\delta,i_0+1}^\pm$ , labeled  $\gamma_{i_0+1}$ , closest to the intersection points between  $\Pi_{i_0+1}$  and the  $\xi_2$ -line(s) (in the sense described in Sec. VB).
- (4) Keep repeating step 3, going through all reference planes that contain closed orbits of  $\eta_{\delta,i}^\pm$ . At the end, use the data points given by the collection of closed orbits  $\{\gamma_i\}$  of the  $\eta_{\delta,i}^\pm$ -fields to interpolate a smooth surface  $\mathcal{M}_\Delta(t_0)$ . If this is not possible, go back to  $\Pi_{i_0}$  and repeat the selection procedure from another available closed orbit of  $\eta_{\delta=0,i_0}^\pm$ .

For both the steady and the time-aperiodic ABC-type flow analyzed here (cf. Sec. VI), the elliptic LCS traverses the entire flow domain along the  $z$ -direction, and we find closed orbits of  $\eta_{\delta,i}^\pm$  on all the reference planes  $\Pi_i$ . The extraction algorithm listed here can, however, handle the more generic case. That is, if the LCS does not span across the whole flow domain, our procedure terminates and produces a shorter LCS: By the end of *part 1*, for all the reference planes  $\Pi_{i=1,2,3,\dots}$ , we have computed a collection of closed orbits of the  $\eta_{\delta,i}^\pm$  vector fields. Assume that for some index  $i^*$ , no nearby closed orbit of the vector field  $\eta_{\delta,i^*}^\pm$  in the plane  $\Pi_{i^*}$  is available. This prevents us from carrying out step 3 of *part 2* for  $i^*$ , and hence our LCS construction procedure terminates.

Overall, the method described here is computationally costly. It is therefore not suitable for running quick diagnostics, but designed to yield results at a very high level of detail. The computational cost is, however, not vastly greater than the cost of computing the FTLE field (*part 1*, step 2): The extra effort is mostly required by the handling of the data produced by the algorithm, rather than by the additional computational steps.

### APPENDIX H: NUMERICAL DETAILS FOR THE EXAMPLES

The numerical settings listed here apply to all three examples: the steady ABC flow over  $[t_0, t] = [0, 40]$  and  $[0, 250]$ , and the time-aperiodic ABC-type flow over  $[0, 40]$ .

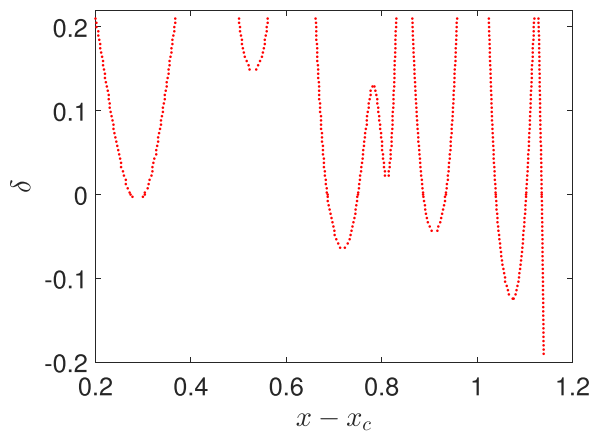


FIG. 17. Steady ABC flow analyzed over  $[t_0, t] = [0, 40]$ : Values of  $\delta$  for the closed orbits of  $\eta_{\delta,1}^{\pm}$  shown in Fig. 5, plotted over the  $x$ -coordinate of their intersections with the Poincaré section  $(x - x_c, 4.73, 0.0)$ , where  $x_c = 3.73$ .

For the computation of  $C_{t_0}^t$ , in each reference plane  $\Pi_i$ , we define a square main grid of  $1000 \times 1000$  points and place initial conditions with relative spacing  $d = 10^{-5}$ . For searching closed orbits of  $\eta_{\delta,i}^{\pm}$ , in each plane  $\Pi_i$ , we use a Poincaré section parallel to the  $x$ -axis at  $y = 4.73$  and place initial conditions for  $\eta_{\delta,i}^{\pm}$ -orbits at a uniform spacing  $\Delta x = 0.002$ . We allow for up to 10 bisection iterations, with an absolute error bound of  $10^{-4}$ . All integrations of differential equations are performed by a Runge-Kutta (4,5) method<sup>5</sup> combined with an adaptive stepper whose absolute and relative error tolerances we set to  $10^{-8}$ .

For the steady ABC flow analyzed over  $[0, 40]$ , we obtain 591 closed orbits of  $\eta_{\delta,1}^{\pm}$  in  $\Pi_1$ . We identify these closed orbits of  $\eta_{\delta,1}^{\pm}$  (cf. Fig. 5) by their intersection points with the Poincaré section at  $y = 4.73$  and plot their  $\delta$ -values in Fig. 17. In our scans of the remaining reference planes  $\Pi_2, \dots, \Pi_{100}$ , we find between 547 and 775 closed orbits.

<sup>1</sup>V. I. Arnol'd and B. A. Khesin, *Topological Methods in Hydrodynamics* (Springer, 1998), Vol. 125, pp. 69–73.

<sup>2</sup>D. Blazeovski and G. Haller, “Hyperbolic and elliptic transport barriers in three-dimensional unsteady flows,” *Physica D* **273–274**, 46–62 (2014).

<sup>3</sup>M. Budisic and I. Mezic, “Geometry of the ergodic quotient reveals coherent structures in flows,” *Physica D* **241**(15), 1255–1269 (2012).

<sup>4</sup>T. Dombre, U. Frisch, J. M. Greene, M. Henon, A. Mehr, and A. M. Soward, “Chaotic streamlines in the ABC flows,” *J. Fluid Mech.* **167**, 353–391 (1986).

<sup>5</sup>J. R. Dormand and P. J. Prince, “A family of embedded Runge-Kutta formulae,” *J. Comput. Appl. Math.* **6**(1), 19–26 (1980).

<sup>6</sup>R. E. Ecke, “Chaos, patterns, coherent structures, and turbulence: Reflections on nonlinear science,” *Chaos* **25**(9), 097605 (2015).

<sup>7</sup>M. Farazmand, D. Blazeovski, and G. Haller, “Shearless transport barriers in unsteady two-dimensional flows and maps,” *Physica D* **278–279**, 44–57 (2014).

<sup>8</sup>M. Farazmand and G. Haller, “Computing Lagrangian coherent structures from their variational theory,” *Chaos* **22**(1), 013128 (2012).

<sup>9</sup>M. Farazmand and G. Haller, “Polar rotation angle identifies elliptic islands in unsteady dynamical systems,” *Physica D* **315**, 1–12 (2016).

<sup>10</sup>S. Friedlander and M. M. Vishik, “Instability criteria for the flow of an inviscid incompressible fluid,” *Phys. Rev. Lett.* **66**, 2204–2206 (1991).

<sup>11</sup>G. Froyland and K. Padberg, “Almost-invariant sets and invariant manifolds—Connecting probabilistic and geometric descriptions of coherent structures in flows,” *Physica D* **238**(16), 1507–1523 (2009).

<sup>12</sup>H. Goldstein, C. P. Poole, and J. L. Safko, *Classical Mechanics*, 3rd ed. (Addison Wesley, San Francisco, 2002), pp. 54–63, 589–600.

<sup>13</sup>A. Hadjighasem and G. Haller, “Geodesic transport barriers in Jupiter’s atmosphere: A video-based analysis,” *SIAM Rev.* **58**(1), 69–89 (2016).

<sup>14</sup>A. Hadjighasem, D. Karrasch, H. Teramoto, and G. Haller, “A spectral clustering approach to Lagrangian vortex detection,” *Phys. Rev. E* (submitted); preprint [arXiv:1506.02258](https://arxiv.org/abs/1506.02258) (2015).

<sup>15</sup>G. Haller, “A variational theory of hyperbolic Lagrangian coherent structures,” *Physica D* **240**(7), 574–598 (2011).

<sup>16</sup>G. Haller, “Lagrangian coherent structures,” *Annu. Rev. Fluid Mech.* **47**(1), 137–162 (2015).

<sup>17</sup>G. Haller and F. J. Beron-Vera, “Coherent Lagrangian vortices: The black holes of turbulence,” *J. Fluid Mech.* **731**, R4 (2013).

<sup>18</sup>G. Haller, A. Hadjighasem, M. Farazmand, and F. Huhn, “Defining coherent vortices objectively from the vorticity,” *J. Fluid. Mech.* (in press); preprint [arXiv:1506.04061v2](https://arxiv.org/abs/1506.04061v2) (2016).

<sup>19</sup>F. Huhn, W. M. van Rees, M. Gazzola, D. Rossinelli, G. Haller, and P. Koumoutsakos, “Quantitative flow analysis of swimming dynamics with coherent Lagrangian vortices,” *Chaos* **25**(8), 087405 (2015).

<sup>20</sup>D. Karrasch, “Attracting Lagrangian coherent structures on Riemannian manifolds,” *Chaos* **25**(8), 087411 (2015).

<sup>21</sup>T. Komatsuzaki and R. S. Berry, “Regularity in chaotic reaction paths. I. Ar6,” *J. Chem. Phys.* **110**(18), 9160–9173 (1999).

<sup>22</sup>M. R. Mazloff, P. Heimbach, and C. Wunsch, “An eddy-permitting Southern Ocean State Estimate,” *J. Phys. Oceanogr.* **40**(5), 880–899 (2010).

<sup>23</sup>J. C. McWilliams, *Fundamentals of Geophysical Fluid Dynamics* (Cambridge University Press, 2006).

<sup>24</sup>K. A. Mitchell and J. R. Mahoney, “Invariant manifolds and the geometry of front propagation in fluid flows,” *Chaos* **22**(3), 037104 (2012).

<sup>25</sup>M. J. Olascoaga and G. Haller, “Forecasting sudden changes in environmental pollution patterns,” *Proc. Natl. Acad. Sci.* **109**(13), 4738–4743 (2012).

<sup>26</sup>J. Oprea, *The Mathematics of Soap Films: Explorations with Maple®* (American Mathematical Society, 2000).

<sup>27</sup>K. L. Palmerius, M. Cooper, and A. Ynnerman, “Flow field visualization using vector field perpendicular surfaces,” in *Proceedings of the 25th Spring Conference on Computer Graphics* (ACM, 2009), pp. 27–34.

<sup>28</sup>I. I. Rypina, L. J. Pratt, P. Wang, T. M. Özgökmen, and I. Mezic, “Resonance phenomena in a time-dependent, three-dimensional model of an idealized eddy,” *Chaos* **25**(8), 087401 (2015).

<sup>29</sup>M. Schulze, C. Rossl, T. Germer, and H. Theisel, “As-perpendicular-as-possible surfaces for flow visualization,” in *2012 IEEE Pacific Visualization Symposium (PacificVis)* (IEEE, 2012), pp. 153–160.

<sup>30</sup>M. Spivak, *A Comprehensive Introduction to Differential Geometry*, 3rd ed. (Publish or Perish, Inc., Houston, Texas, 1999), Vol. 4, pp. 259–313.

<sup>31</sup>Y. Wang, M. J. Olascoaga, and F. J. Beron-Vera, “Coherent water transport across the South Atlantic,” *Geophys. Res. Lett.* **42**(10), 4072–4079, doi:10.1002/2015GL064089 (2015).